Correlation between Micro-Scale Magnetic Particle Distribution and Magnetic-Field-Responsive Performance of 3D Printed Composites

Article *in* Journal of Micro and Nano-Manufacturing · November 2017

DOI: 10.1115/1.4038574

3 authors, including:

Lu Lu
University of Illinois at Chicago
13 PUBLICATIONS **60** CITATIONS

SEE PROFILE

Correlation Between Microscale Magnetic Particle Distribution and Magnetic-Field-Responsive Performance of Three-Dimensional Printed Composites

Lu Lu
Mem. ASME
Department of Mechanical and Industrial Engineering,
University of Illinois at Chicago,
842 W Taylor Street, ERF 1076,
Chicago, IL 60607
e-mail: llu27@uic.edu

Erina Baynojir Joyee
Mem. ASME
Department of Mechanical and Industrial Engineering,
University of Illinois at Chicago,
842 W Taylor Street, ERF 1076,
Chicago, IL 60607
e-mail: ejoyee2@uic.edu

Yayue Pan[1]
Mem. ASME
Department of Mechanical and Industrial Engineering,
University of Illinois at Chicago,
842 W Taylor Street, ERF 1076,
Chicago, IL 60607
e-mail: yayuepan@uic.edu

To date, several additive manufacturing (AM) technologies have been developed for fabricating smart particle–polymer composites. Those techniques can control particle distributions to achieve gradient or heterogeneous properties and functions. Such manufacturing capability opened up new applications in many fields. However, it is still widely unknown how to design the localized material distribution to achieve desired product properties and functionalities. The correlation between microscale material distribution and macroscopic composite performance needs to be established. In our previous work, a novel magnetic field-assisted stereolithography (M-PSL) process was developed, for fabricating magnetic particle–polymer composites. In this work, we focused on the study of magnetic-field-responsive particle–polymer composite design with the aim of developing guidelines for predicting the magnetic-field-responsive properties of the composite. Microscale particle distribution parameters, including particle loading fraction, magnetic particle chain structure, microstructure orientation, and particle distribution patterns, were investigated. Their influences on the properties of particle–polymer liquid suspensions and properties of the three-dimensional (3D) printed composites were characterized. By utilizing the magnetic anisotropy properties of the printed composites, motions of the printed parts could be actuated at different positions in the applied magnetic field. Physical models were established to predict magnetic properties of the composite and trigger distance of fabricated parts. The predicted results agreed well with the experimental measurements, indicating the effectiveness of predicting macroscopic composite performance using microscale distribution data, and the feasibility of using the developed physical models to guide multimaterial and multifunctional composite design. [DOI: 10.1115/1.4038574]

1 Introduction

By combining various materials that serve mechanical, electrical, chemical, thermal, and/or optical functions with controlled distributions at microscale in the polymer matrix, smart particle–polymer composite with multiple functionalities can be fabricated [1–18]. Transformative applications have been demonstrated in targeted drug delivery, micromachines, microelectromechanical systems, by using the advanced characteristics of such particle–polymer composite [3–13]. Four examples of the smart composite applications are: (a) a self-folding microgripper, which consists of flexible polymer hinges and rigid Au/Ni phalanges, for collecting tissue samples from porcine liver [3]; (b) a soft reconfigurable connector fabricated by filling magnetically oriented platelets in the soft polymer, which changes shape under an external magnetic field [5]; (c) a microfish, which has iron oxide and platinum nanoparticles embedded in the polymer matrix at different regions, for targeted drug delivery and toxin-neutralization applications [4]; (d) a mesoscale turbo fan, which has iron particles embedded on its blade tips and can rotate with various rotation speeds under an external magnetic field [9].

Various novel manufacturing technologies have been developed to fabricate such smart materials. A simple one-exposure in situ fabrication approach was developed by Kwon and coworkers, and they successfully fabricated magnetic actuators, which consist of magnetic and nonmagnetic components [19,20]. Additive manufacturing (AM), also known as three-dimensional (3D) printing, is a class of new manufacturing technologies that fabricate 3D models by accumulating materials, from the bottom to the top, usually in a layer-by-layer way. Compared to conventional manufacturing techniques, it has many advantages such as design freedom, assembly free, and little material waste. Erb and coworkers developed a 3D magnetic printing process and demonstrated successful productions of complex bioinspired reinforcement architectures using magnetic microplatelets and polymer [21]. The 3D magnetic printing process proposed by Erb et al. applies a magnetic field via electromagnetic solenoids simultaneously with digital mask image photo-polymerization of liquid resin. In this manufacturing process, orientations of magnetic microplatelets could be manipulated and controlled in a three-dimensional part, in layers and between layers. In addition, Studart and coworkers developed another magnetically assisted 3D printing technique for fabricating magnetic-field-responsive particle–polymer composites [5]. Their 3D printing technique is based on direct ink writing process, in which magnetic platelets and resin are mixed and dispensed through nozzles, while a magnet is used to orient the magnetic platelets. In this process, both the magnetic platelet loading fraction and orientation can be controlled in a layer-by-layer way. In our previous study, we developed a new additive manufacturing process, magnetic-field-assisted projection stereolithography (M-PSL), and demonstrated its capability of fabricating particle–polymer composites with various particle distributions and product properties [9]. In the developed M-PSL process,

[1]Corresponding author.

Contributed by the Manufacturing Engineering Division of ASME for publication in the Journal of Micro- and Nano-Manufacturing. Manuscript received June 17, 2017; final manuscript received November 20, 2017; published online December 14, 2017. Assoc. Editor: Nicholas Fang.

magnetic particles can be filled into the polymer matrix with different orientations, structured chains, and loading fractions to achieve varied composite properties and product functionalities.

Despite the progress in advanced manufacturing techniques, significant challenges exist in the design of the multimaterial part to achieve the desired functionalities. It is still largely unknown how to blend materials at the microscale level to obtain the desired macroscopic performance of the printed part. With the traditional design methods and knowledge that are mainly established for single-material part manufacturing, it is not clear how to design particle distributions to achieve the desired performance of the final printed product. For design of magnetic particle–polymer composites, Kwon and coworkers investigated how to obtain desired magnetic torque by spatially controlling magnetic particle dispersion patterns [20]. They modeled the magnetic torque to a single chain and designed microactuators driven by the heterogeneous magnetic anisotropy. Doyle and coworkers investigated the chain structures formed when magnetic particles in liquid resin are subjected to a uniform magnetic field, providing a basis for understanding the magnetorheological (MR) suspensions [22].

In this work, we focused on the study of magnetic particle–polymer composite design with the aim of developing guidelines for predicting the magnetic-field-responsive properties of the 3D printed composite fabricated by M-PSL process. Microscale particle distribution parameters, including particle loading fraction, magnetic particle chain structure, microstructure orientation, and distribution patterns, were investigated. Their influences on macroscopic composite performance were characterized. By utilizing the magnetic anisotropy properties of the printed composites, motions of the printed parts could be actuated at different relative positions in the applied magnetic field. By revealing the correlation between microscopic magnetic particle distribution and macroscopic composite responses to a magnetic field, we would be able to design the magnetic particle–polymer composite properly and predict trigger condition for printed parts.

Section 2 reviews the magnetic field-assisted projection stereolithography process developed in our previous work for composite fabrication [7]. In addition, three sets of samples, with different microscale particle distribution properties, were designed and then fabricated using M-PSL. Section 3 characterizes the microscale distribution characteristics and macroscopic performances of the fabricated samples, and discusses effects of particle distribution on magnetic-field-responsive properties of printed composite. Analytic models were developed and experiments were performed to analyze the macroscopic performances, including trigger distance and magnetic anisotropy properties. Finally, conclusions and future work were given in the end.

2 Magnetic-Field-Responsive Composite Fabrication

2.1 Magnetic Field-Assisted Projection Stereolithography Process Overview. The magnetic field-assisted projection stereolithography system is illustrated in Fig. 1. It integrates a conventional bottom-up projection stereolithography setup with a drop-on-demand dispensing system as well as an external magnetic field. Key components include an imaging unit, a resin vat, a linear actuator for elevating the build platform in Z direction, and a magnet mounted on a rotational stage. The resin vat can slide on the X–Y plane driven by two linear stages. All four axes are controlled by one controller. First, sliced images from a 3D computer-aided design model of the object are converted to digital mask images. Next, the dispensing system deposits magnetic particles into the resin vat. Furthermore, by controlling the motion path of a magnet beneath the resin vat, magnetic particles can be guided to desired areas before the resin curing. Then the digital mask image will be projected by the imaging unit to the bottom of the resin vat for solidification. By repeating this procedure, magnetic particle–polymer composites can be fabricated. The external magnetic field can control particle dispersion patterns and local distribution ratios. This multimaterial additive manufacturing process can achieve fast build speed, local magnetic intelligence, and fabrication of composites with heterogeneous properties. A prototype machine has been developed to implement fabrication process for particle–polymer composites. Process parameter settings were investigated and optimized in our previous study [23]. The appropriate layer thickness and curing time were selected based on our previous study of the relationship between the curing depth and the magnetic particle loading fraction [23]. During the curing process, the light is absorbed by magnetic particles in the suspension. As the loading fraction of the magnetic particles increases, the curing depth decreases. As a result, a smaller layer thickness or a longer curing time is used in our manufacturing process for curing layers with higher volume loading fraction of magnetic particles.

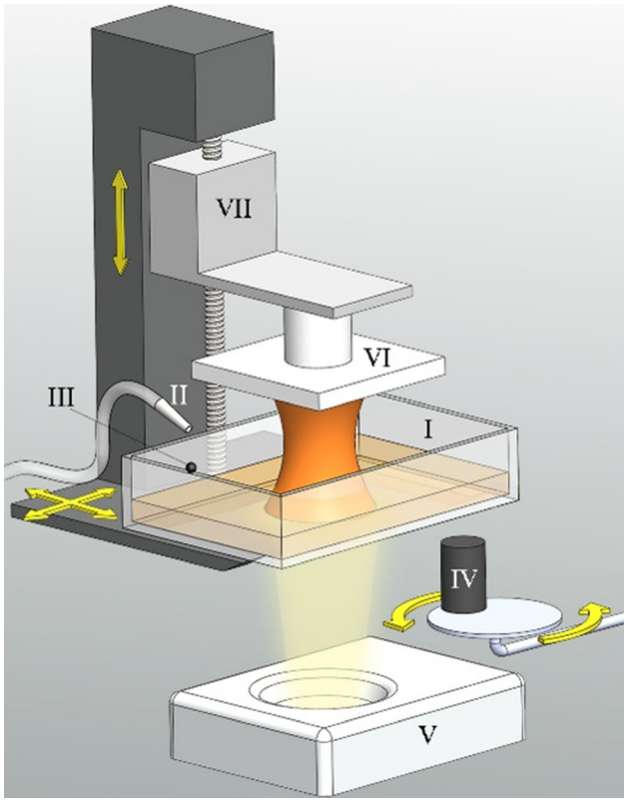

Fig. 1 A schematic diagram of the smart polymer composite printing system using M-PSL process. (I) Resin vat (II) microscaled nozzle (III) particle droplet (IV) magnet (V) image unit (VI) platform (VII) linear actuator.

2.2 Printed Results. Photopolymer 3DM-ABS (3D Materials, Inc., Soultz-Haut-Rhin, France) and magnetorheological fluid LORD MRF-122EG (Mid-Atlantic Rubber, Inc., Baltimore, MD) were used to fabricate samples discussed in Sec. 3. Suspension samples with six various MR fluid volume loading fractions from 5.7% to 11.5% were prepared by mixing resin and MR fluid. All suspension samples were homogenized by using Thinky AR-100 Conditioning Mixer and then were used as the feedstock. Three sets of samples were fabricated using M-PSL process. Pictures of a fabricated sample in set-0 (S0), a sample in set-1 (S1), and set-2 (S2) samples are shown in Fig. 2. These three sets of samples were numbered orderly according to the microscale particle distribution complexity, and described in Sec. 3.

Set-0 (S0) samples are polymer composites filled with nonstructured particles. Six samples were printed by mixing MR fluid with liquid resin uniformly with varied MR fluid volume loading fractions, 5.7%, 6.6%, 7.5%, 8.5%, 9.8%, and 11.5%, and then curing the suspension in the absence of magnetic field. Figure 2(*a*) shows a printed sample with 8.5% loading fraction. Due to the uniform mixing

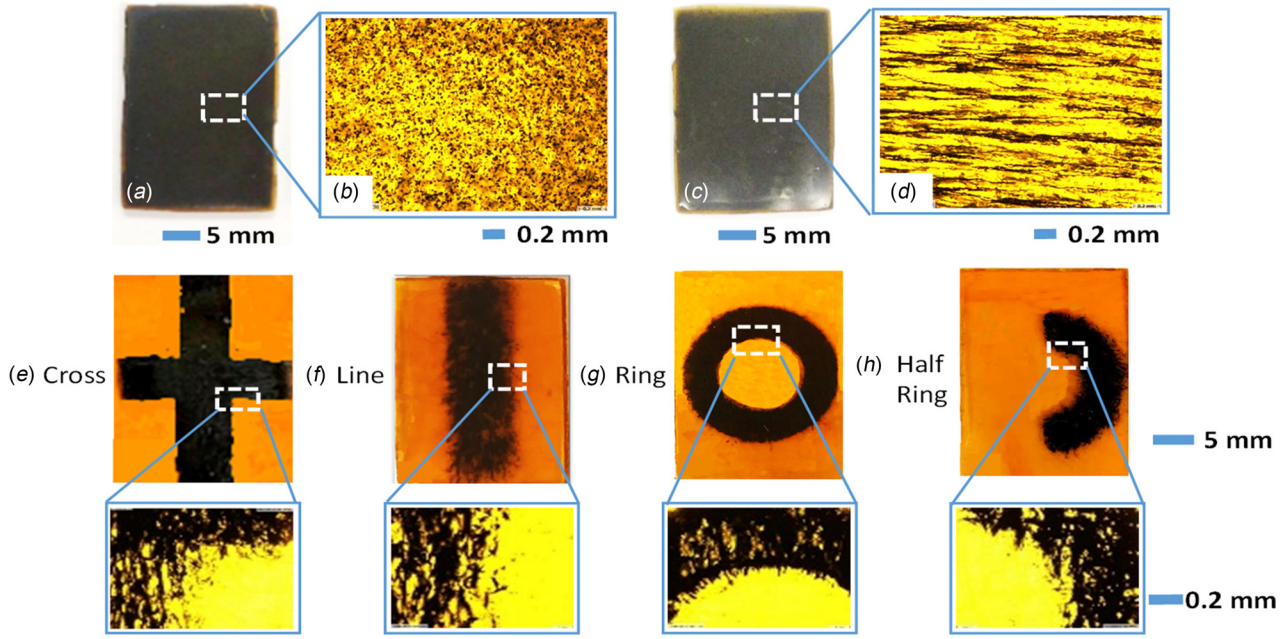

Fig. 2 (*a*) and (*b*) A printed sample in set-0. (*c*) and (*d*) A printed sample in set-1. (*e*)–(*h*) Printed samples in set-2.

of magnetic particles and the base liquid resin, the printed composite contains randomly dispersed black particles as shown in Fig. 2(*a*). Under microscope, we can observe the uniformly distributed magnetic particles in polymer matrix, as shown in Fig. 2(*b*).

By applying a uniform magnetic field during the printing process, magnetic particles were magnetically directed and formed into chain-like structures, which roughly aligned with the magnetic field induction line. After photo-curing, chain structures were locked inside the polymer matrix. Six magnetic particle chain-polymer composite samples with different MR fluid volume loading fractions, 5.7%, 6.6%, 7.5%, 8.5%, 9.8%, and 11.5%, were fabricated. These samples are grouped as set-1 (S1) samples. Figure 2(*c*) shows a printed S1 sample with 8.5% loading fraction, and Fig. 2(*d*) shows its microscopic image. The chain structure of magnetic particles can be easily observed in Fig. 2(*d*).

For set-2 (S2) samples, composites with particle chains dispersed with patterns in the polymer matrix were fabricated. Four distribution patterns were tested, including cross, line, ring, and half ring. Pictures of printed part and the related microscopic images are shown in Figs. 2(*e*)–2(*h*). The black region is particle chain embedded, while the yellow region is pure polymer. We defined the local loading fraction as the volume of the magnetic particles over the volume covered by the pattern, and the overall loading fraction as the volume of the magnetic particles over the volume of the printed part. For cross pattern and line pattern, they have the same overall volume loading fraction 2.7% but different local volume loading fraction, 7.0% for cross pattern and 6.0% for the line pattern. The ring and half ring patterned samples have the same overall volume loading fraction 0.6%, but different local loading fractions, 6.5%, and 9.4%, respectively.

After fabricating these three sets of samples, experiments were designed and conducted to study the effects of different microscale particle distribution factors on magnetic-field-responsive properties of the fabricated particle–polymer composites, including trigger distance and magnetic flux density.

3 Results and Discussions

3.1 Trigger Distance Prediction and Validation

3.1.1 Modeling. As known, magnetic force F_M exerted on the printed composites in an applied magnetic field can be expressed by the following equation from Coulomb's law for magnetism:

$$F_M = \frac{\mu_0 q_{m1} q_{m2}}{4\pi d^2} \tag{1}$$

where μ_0 is the vacuum permeability, q_{m1} and q_{m2} are the magnitudes of magnetic poles of the magnet and the printed sample, respectively, and d is the distance between the sample and the magnet.

The trigger distance is defined as the maximum distance at which the magnet can actuate the motion of the part. As a critical threshold for remote control, the trigger distance plays an important role in determining the magnetic-field-responsive performance of the 3D printed composite. Accurate prediction of the trigger distance before fabrication provides guideline for composites component design. The trigger distance d_t could be obtained by balancing gravity with magnetic force F_M. The magnitude of magnetic poles is given by

$$q_m = \frac{MV}{L} \tag{2}$$

where M is the magnetization, V is the volume, and L is the characteristic length.

By setting the sample weight W_S equivalent to the magnetic force F_M and using Eqs. (1) and (2), the trigger distance d_t can be derived as below:

$$d_t = \left(\frac{\mu_0 q_{m1} M_s V_s}{4\pi L_s W_s}\right)^{\frac{1}{2}} \tag{3}$$

where M_s is the saturation magnetization of the liquid suspension, V_s is the sample volume, L_s is the sample characteristic length, and W_s is the sample weight.

Furthermore, as the magnetic field increases, the particle magnetization increases toward saturation, which introduces changes in the viscosity and the appearance of yield stress in the mixed suspension. Yield stress represents the point where the transmission from solid-like to liquid-like happens. With a stress larger than the yield stress, the suspension starts to flow. Yield stress dependence of the applied magnetic field becomes subquadratic. In addition, there is a linear dependency of yield stress on the volume loading fraction of the MR fluid [24,25]. Accordingly, the saturation magnetization of the suspension can be modeled as

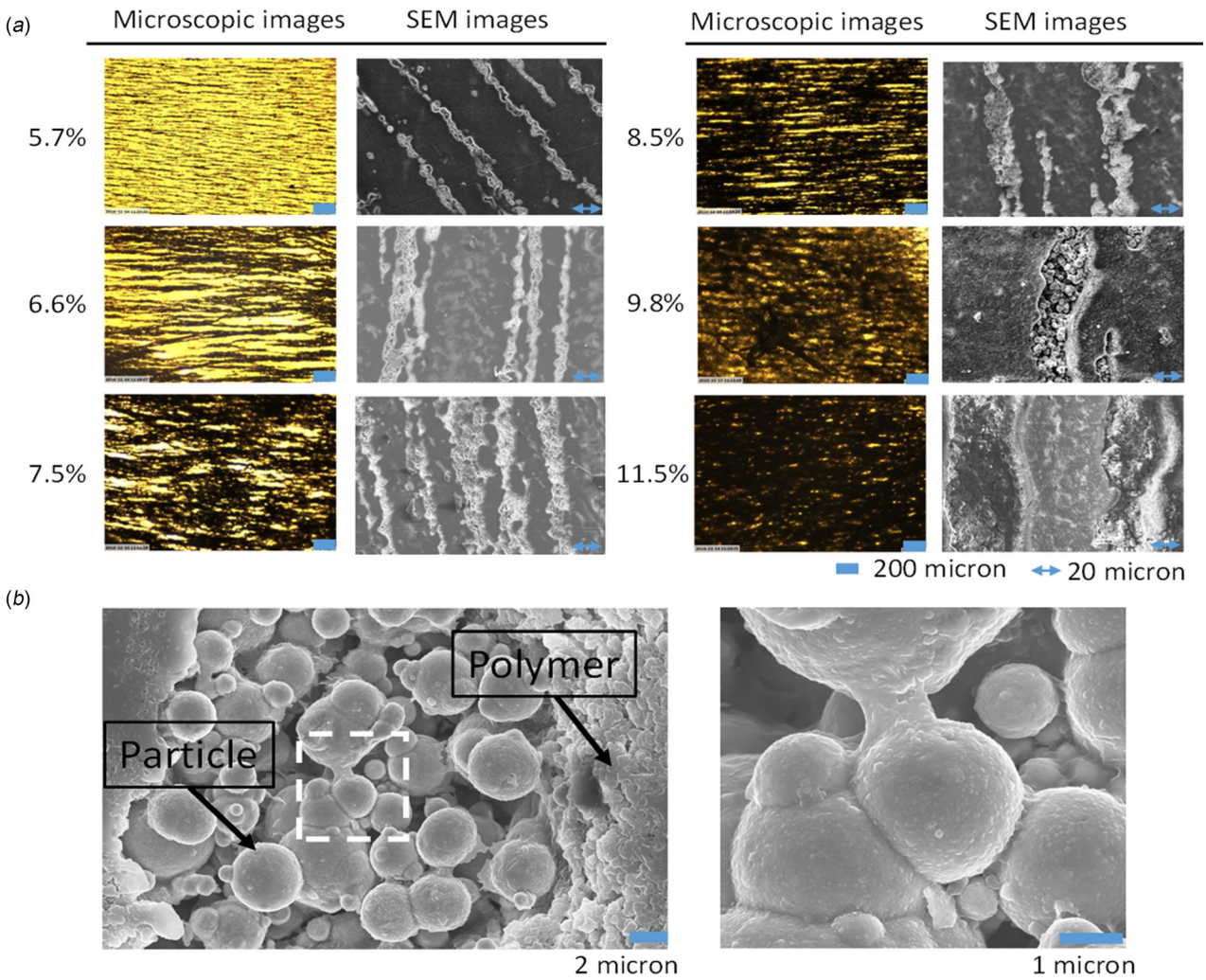

Fig. 3 Cured single layer sample: (*a*) microscopic images and SEM images of cured thin pieces and (*b*) SEM of the chain structure

$$M_s = \frac{\tau_{ys}^2}{6\varphi^2\mu_0^2 H^3} \tag{4}$$

where τ_{ys} represents the yield stress, φ is the volume loading fraction of MR fluid, and H is the applied magnetic field.

It is assumed that the saturation magnetization of the liquid sample and the cured piece are very close, because it is observed that the magnetic property of magnetic particles did not change after solidification. Therefore, trigger distance can be rewritten in the expression listed below:

$$d_t = \left(\frac{q_{m1}V_s}{24\pi\mu_0 L_s W_s \varphi^2 H^3}\right)^{\frac{1}{2}} \tau_{ys} \tag{5}$$

Since terms inside brackets are known, after finding out yield stress of the liquid suspension samples, trigger distance can be predicted easily. The yield stress depends on particle size, composition, and magnetization saturation of particles [26].

3.1.2 Effects of Microstructure on Rheological Characteristics of S0 and S1 Suspensions. To observe the microstructures of these suspensions, a thin circular layer with a thickness of 0.1 mm was cured by a UV lamp. Then the microstructures were observed with a precision measurement system from Micro-Vu Inc., Windsor, CA. Figure 3 shows the observed microstructures of formed magnetic chains, with different MR fluid volume loading fractions. Figure 3(*b*) gives a closer view of the chain structures. The particle chain is embedded in the polymer matrix. Inside the chain, particles are coated by a thin layer of resin, which bonded the particles together. Due to the magnetization, the magnetic particles attracted one another forming chain-like structures that in turn join to form columnar structures. Those chains had unidirectional alignment with the magnetic field induction line because of polarization. With increased particle volume loading fraction, particle chain distributions were denser. From scanning electron microscope (SEM) images, the formed chains were wider as the volume loading fraction of particles increase. Such a chain dimension change would cause changes in suspension rheological properties and performances of the printed composites under magnetic field.

Rheological properties of suspensions with varied magnetic particle loading fractions were characterized at 25 °C using a Malvern Kinexus ultra+ rotational rheometer from Malvern Instruments Ltd., Malvern, UK. The measurements were carried out both in the absence of magnetic field and with a magnetic field of 1592 A/m, and involved a logarithmic increase of the shear stress from 0.1 to 100 Pa.

The base resin is a typical Newtonian fluid with a linear relation between the shear rate and the shear stress, as shown in Fig. 4(*a*). The commercial Lord MR fluid behaves as a shear thickening fluid with the increased shear rate in Fig. 4(*b*). The first set of measurements was conducted without the magnetic field. As the shear stress–shear rate plot is shown in Fig. 4(*c*), all suspensions behave

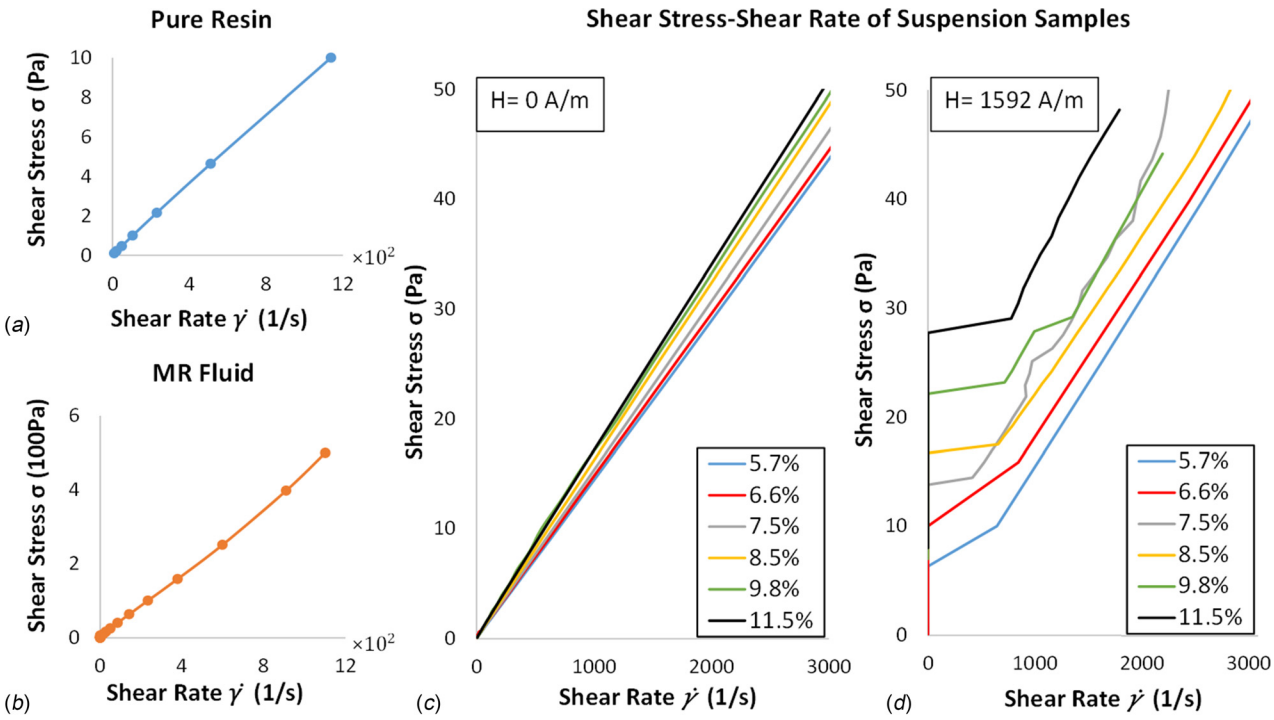

Fig. 4 Shear stress–shear rate plot: (*a*) pure resin, (*b*) pure MR fluid, (*c*) suspension samples without magnetic field, and (*d*) suspension sample with magnetic field

as Newtonian flow. It indicates that the base resin dominates the suspension rheological property. In the second set of experiments, a magnetic field with strength of 1592 A/m was applied during measurements. With the presence of the magnetic field, all the suspension samples exhibit Bingham plastic behaviors as shown in Fig. 4(*d*). The intersections on the stress axis are identified as the yield stresses. The nonvanishing yield stresses imply the formation of stable chain structures of magnetized particles. The result shows that both the yield stress and the chain width increased with the order of increasing particle volume loading fraction. Additionally, thicker chains lead to a larger yield stress.

From Fig. 4, the loading fraction of structured magnetic particles is the critical parameter that defines rheological properties of the composite fluids. Even a small number of magnetic particles in the suspension would induce particle attraction to form into chain structures under an external magnetic field, thereby completely changing the viscoelastic properties of the suspension.

3.1.3 Prediction of Saturation Magnetization of S1 Samples. As shown in Eq. (4), the saturation magnetization of each suspension sample can be calculated by using the yield stress of suspensions. We assumed that the saturation magnetization of printed parts can be estimated using the suspension saturation magnetization. To test this assumption, the saturation magnetizations of printed samples were calculated using the yield stress shown in Fig. 4(*d*) and then compared with the magnetization directly measured by F.W. bell 5170 Gaussmeter (Berg Engineering Inc., Rolling Meadows, IL). In Fig. 5(*a*), red crosses denote predicted saturation magnetizations, and blue squares represent magnetizations measured directly by the Gaussmeter. The predicted values agree very well with the measured values. Accordingly, it can be concluded that measured yield stress of suspensions could be used to predict saturation magnetizations of printed composites in the S1 group. It should be noted that although the prediction model is monotonic, measured data from Fig. 4(*d*) are used for the yield

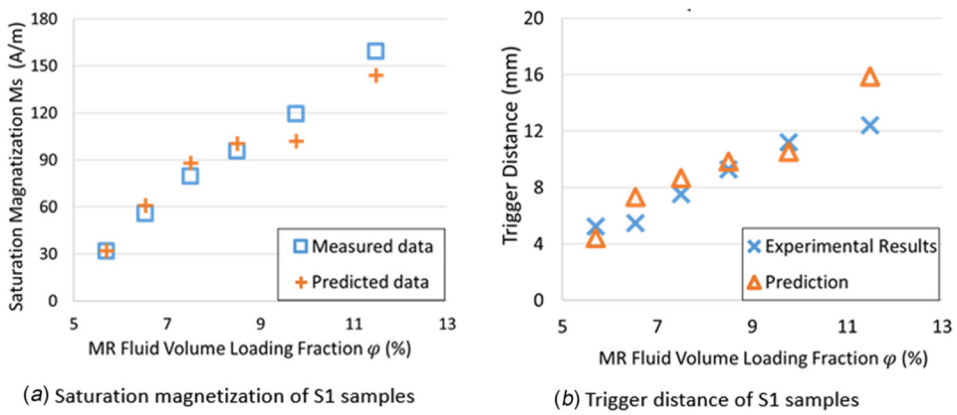

Fig. 5 Comparison between experimental data and prediction: (*a*) saturation magnetization and (*b*) trigger distance

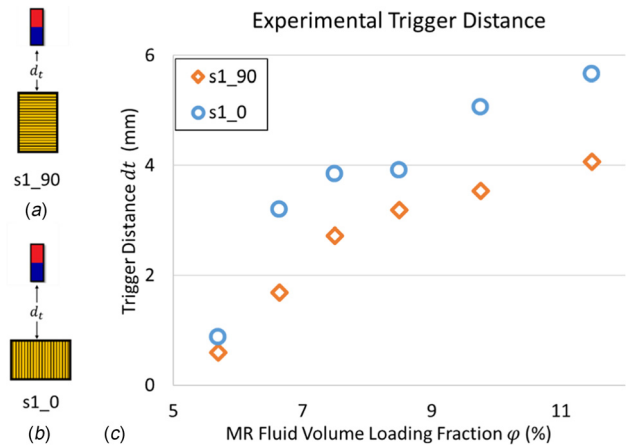

Fig. 6 Experimental trigger distance with different chain orientations

stress τ_{ys} in the model. The use of such measured data in the prediction model causes the fluctuation of predicted magnetizations as shown in Fig. 5(*a*).

3.1.4 Prediction of Trigger Distance of S1 Samples. As seen in Eq. (5), trigger distance of S1 samples can be predicted based on the saturation magnetization obtained from magnetorheological properties of liquid samples. To validate the prediction, experiments were conducted to measure the trigger distance. First, a magnet was placed on the top of a flatly placed sample. Then it slowly approached the printed part. As the distance decreases, eventually, the part would be attracted to the magnet. The distance, where the part started to move, was recorded as the experimental trigger distance.

As shown in Fig. 5(*b*), the predicted trigger distances agree well with the experimental results. The average prediction error for six samples was 9%. It is verified that accurate prediction of trigger condition could be obtained from magnetorheological properties of the composite fluids, using Eq. (5).

3.1.5 Effects of Chain Orientation on Trigger Distance of S1 Samples. To study effects of chain orientations on trigger distance, S1 sample was placed vertically in two orientations, with which chain structures were perpendicular to the magnetic induction line (denoted as s1_90) and were parallel to it (denoted as s1_0), as shown in Figs. 6(*a*) and 6(*b*). The results were plotted in Fig. 6(*c*). When the chain orientation was parallel to the magnetic field induction line, it exerted larger magnetic force than perpendicular orientation, resulting in a longer trigger distance.

3.2 Magnetic Anisotropy Properties of Printed Composites. Magnetic flux density, also known as magnetic induction, is another significant magnetic-field-responsive property. In this paper, magnetic flux density was experimentally studied to investigate the magnetic anisotropy properties of the printed composite. A highly accurate and sensitive MilliGaussmeter IDR-322 was used for measuring the magnetic flux density of each sample at different location on it. To measure the minuscule value of magnetic field density, the smallest range 4 mG was chosen to get a very accurate measurement. A chamber made of GIRON magnetic shielding film was used for eliminating the environmental magnetic field effects. All experiments were conducted inside this chamber.

The probe of MilliGaussmeter IDR-322 is an axial hall probe. Consequently, when the probe is placed in a magnetic field, it measures the magnetic field in that direction, and the maximum reading occurs when the axis of the probe is parallel to the magnetic field. The hall generator (sensor) is in the middle of the probe. Measurements of three points at different locations of printed samples were chosen to analyze the magnetic flux density at various areas on the printed parts. As illustrated in Fig. 7(*a*), those three points were: the center point of the sample (s0p1), the

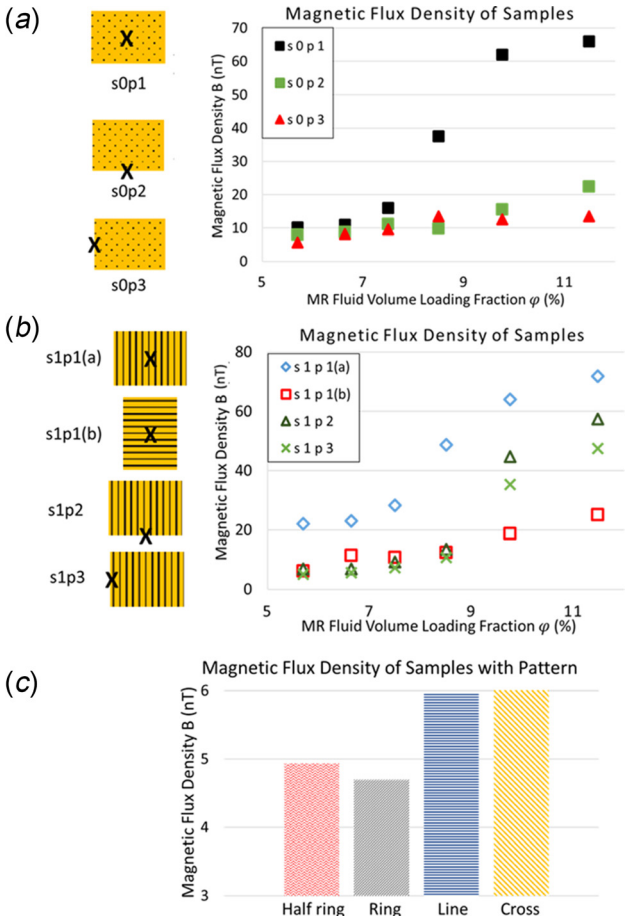

Fig. 7 Magnetic flux density of samples in (*a*) set-0, (*b*) set-1, and (*c*) set-2

middle point of the long edge (s0p2), and the middle point of the short edge (s0p3).

For S0 samples, measurements were plotted in Fig. 7(*a*). The results indicate that the magnetic flux density shows an ascending trend with the increase in the loading fraction of MR fluid. Moreover, s0p1 shows the largest magnetic flux density because it is at the center, where the flux lines are denser and more concentrated. Measurement of s0p2 is slightly higher than s0p3, because it locates on the axis of the axially magnetized part.

For S1 samples, measurements at the center point (s1p1) were taken at two different orientations, which were aligning the gaussmeter probe axis parallel and perpendicular with the chain orientation. They were marked as s1p1(a) and s1p1(b), respectively. The measured data were plotted in Fig. 7(*b*). It is found that findings obtained from S0 sample measurements also applied to S1 samples. The strongest magnetic flux density was found at s1p1(a). Although s1p1(b) is also in the center, measured magnetic flux density is much lower than s1p1(a). In addition, at a low loading fraction range, magnetic flux density measured at s1p1(b) was slightly higher than p2 and p3. However, at a high loading fraction range, s1p2 and s1p3 had much higher magnetic flux density than s1p1(b). It demonstrates that orientations of chain structures affected the magnetic flux density obviously.

Moreover, to investigate the influence of chain dispersion patterns on the magnetic performance of 3D printed parts, magnetic flux densities of S2 samples were also measured. The results were plotted in Fig. 7(*c*). The magnetic flux density was still mainly determined by the overall volume loading fraction, instead of local loading fraction. Higher overall loading fraction means a larger volume of magnetic particles, causing a higher magnetic flux density at the central position of the printed parts. For

samples of ring and half ring distribution patterns with different local loading fractions, although the overall loading fraction was the same, lower local loading fraction exhibits a lower magnetic flux density. It indicates that with the same overall loading fraction, the magnetic properties were affected by the local loading fraction, which is caused by the particle distribution patterns.

4 Conclusions

In this paper, influences of microscopic distribution parameters, including particle loading fraction, magnetic particle chain structures, and orientations, on magnetic-field-responsive properties of the 3D printed composites were modeled and experimentally studied. It was found that with nonstructured magnetic particles, the suspension properties were dominated by the resin, which usually shows Newtonian fluid characteristics. While for structured magnetic particle chains, the particle chain-polymer suspensions exhibit Bingham Plastic characteristics, strongly depending on the particle chain loading fractions and dimensions. Furthermore, it is found that the measured yield stress of suspensions could be used to predict the saturation magnetization of the cured composites accurately. In addition, experimental results showed that the magnetic-field-responsive properties of printed composites with all particle distribution designs were enhanced with increased particle volume loading fraction. However, the magnetic flux densities varied significantly at different locations and orientations. In addition to samples with uniformly distributed particles or chain structures, parts with different particle chain dispersion patterns have also been fabricated and tested. It was found that the overall loading fraction was still the dominant factor on determining the magnetic flux densities of the printed samples. However, with the same loading fraction, the distribution pattern affected the magnetic properties of the composites significantly, through determining the local loading fractions in the part.

Future work will include: (1) further investigate the heterogeneous properties created by complicated distribution patterns, and (2) investigate the influence of microscopic distribution patterns on mechanical properties of the printed composites.

Nomenclature

d = distance
d_t = trigger distance
F_M = magnetic force
H = applied magnetic field
L_s = characteristic length of sample
M_s = saturation magnetization
q_{m1} = magnitudes of magnetic field
q_{m2} = magnitudes of magnetic poles of sample
V_s = volume of sample
W_S = weight of sample
μ_0 = vacuum permeability
τ_{ys} = yield stress
φ = volume loading fraction of MR fluid

References

[1] Zhang, L., Peyer, K. E., and Nelson, B. J., 2010, "Artificial Bacterial Flagella for Micromanipulation," Lab Chip, **10**(17), pp. 2203–2215.
[2] Zhang, L., Abbott, J. J., Dong, L., Peyer, K. E., Kratochvil, B. E., Zhang, H., Bergeles, C., and Nelson, B. J., 2009, "Characterizing the Swimming Properties of Artificial Bacterial Flagella," Nano Lett., **9**(10), pp. 3663–3667.
[3] Leong, T. G., Randall, C. L., Benson, B. R., Bassik, N., Stern, G. M., and Gracias, D. H., 2009, "Tetherless Thermobiochemically Actuated Microgrippers," Proc. Natl. Acad. Sci., **106**(3), pp. 703–708.
[4] Zhu, W., Li, J., Leong, Y. J., Rozen, I., Qu, X., Dong, R., Wu, Z., Gao, W., Chung, P. H., Wang, J., and Chen, S., 2015, "3D-Printed Artificial Microfish," Adv. Mater., **27**(30), pp. 4411–4417.
[5] Kokkinis, D., Schaffner, M., and Studart, A. R., 2015, "Multimaterial Magnetically Assisted 3D Printing of Composite Materials," Nat. Commun., **6**, p. 8643.
[6] Yang, Y., Chen, Z., Song, X., Zhang, Z., Zhang, J., Shung, K. K., Zhou, Q., and Chen, Y., 2017, "Biomimetic Anisotropic Reinforcement Architectures by Electrically Assisted Nanocomposite 3D Printing," Adv. Mater., **29**(11), p. 1605750.
[7] Genovéva, F., Csetneki, I., Szilágyi, A., and Zrínyi, M., 2007, "Magnetic Field-Responsive Smart Polymer Composites," *Oligomers-Polymer Composites-Molecular Imprinting*, Springer, Berlin, pp. 137–189.
[8] Wurm, G., Tomancok, B., Holl, K., and Trenkler, J., 2004, "Prospective Study on Cranioplasty With Individual Carbon Fiber Reinforced Polymer (CFRP) Implants Produced by Means of Stereolithography," Surg. Neurol., **62**(6), pp. 510–521.
[9] Lu, L., Guo, P., and Pan, Y., 2017, "Magnetic-Field-Assisted Projection Stereolithography for Three-Dimensional Printing of Smart Structures," ASME J. Manuf. Sci. Eng., **139**(7), p. 071008.
[10] Vach, P. J., Burn, N., Bennet, M., Bertinetti, L., Widdrat, M., Baumgartner, J., Klumpp, S., Fratzl, P., and Faivre, D., 2013, "Selecting for Function: Solution Synthesis of Magnetic Nanopropellers," Nano Lett., **13**(11), pp. 5373–5378.
[11] Ji, Y. Z., Wang, Z., Wang, B., Chen, Y., Zhang, T., Chen, L. Q., Song, X., and Chen, L., 2017, "Effect of Meso-Scale Geometry on Piezoelectric Performances of Additively Manufactured Flexible Polymer-Pb (Zr_xTi_{1-x}) O_3 Composites," Adv. Eng. Mater., **19**(6), p. 1600803.
[12] Chakraborty, P., Gundrati, N. B., Zhou, C., and Chung, D. D. L., 2017, "Effect of Stress on the Capacitance and Electric Permittivity of Three-Dimensionally Printed Polymer, With Relevance to Capacitance-Based Stress Monitoring," Sens. Actuators, A, **263**, pp. 380–385.
[13] Chabok, H., Zhou, C., Chen, Y., Eskandarinazhad, A., Zhou, Q., and Shung, K., 2012, "Ultrasound Transducer Array Fabrication Based on Additive Manufacturing of Piezocomposites," ASME Paper No. ISFA2012-7119.
[14] Gundrati, N. B., Chakraborty, P., Zhou, C., and Chung, D. D. L., 2017, "Effects of Printing Conditions on the Molecular Alignment of Three-Dimensionally Printed Polymer," Composites, Part B, **134**, pp. 164–168.
[15] Yang, Y., Chen, Z., Song, X., Zhu, B., Hsiai, T., Wu, P. I., Xiong, R., Shi, J., Chen, Y., Zhou, Q., and Shung, K. K., 2016, "Three Dimensional Printing of High Dielectric Capacitor Using Projection Based Stereolithography Method," Nano Energy, **22**, pp. 414–421.
[16] Lin, D., Jin, S., Zhang, F., Wang, C., Wang, Y., Zhou, C., and Cheng, G. J., 2015, "3D Stereolithography Printing of Graphene Oxide Reinforced Complex Architectures," Nanotechnology, **26**(43), p. 434003.
[17] Bartolo, P. J., and Gaspar, J., 2008, "Metal Filled Resin for Stereolithography Metal Part," CIRP Ann., **57**(1), pp. 235–238.
[18] Chen, B., Jiang, Y., Tang, X., Pan, Y., and Hu, S., 2017, "Fully Packaged Carbon Nanotube Supercapacitors by Direct Ink Writing on Flexible Substrates," ACS Appl. Mater. Interfaces, **9**(34), pp. 28433–28440.
[19] Chung, S. E., Kim, J., Choi, S. E., Kim, L. N., and Kwon, S., 2011, "In Situ Fabrication and Actuation of Polymer Magnetic Microstructures," J. Microelectromech. Syst., **20**(1), pp. 785–787.
[20] Kim, J., Chung, S. E., Choi, S. E., Lee, H., Kim, J., and Kwon, S., 2011, "Programming Magnetic Anisotropy in Polymeric Microactuators," Nat. Mater., **10**, pp. 747–752.
[21] Martin, J. J., Fiore, B. E., and Erb, R. M., 2015, "Designing Bioinspired Composite Reinforcement Architectures Via 3D Magnetic Printing," Nat. Commun., **6**, p. 8641.
[22] Rich, J. P., McKinley, G. H., and Doyle, P. S., 2012, "Arrested Chain Growth During Magnetic Directed Particle Assembly in Yield Stress Matrix Fluids," Langmuir, **28**(8), pp. 3683–3689.
[23] Pan, Y., and Lu, L., 2016, "Additive Manufacturing of Magnetic Field-Responsive Smart Polymer Composites," ASME Paper No. MSEC2016-8865.
[24] Ginder, J. M., and Davis, L. C., 1994, "Shear Stresses in Magnetorheological Fluids: Role of Magnetic Saturation," Appl. Phys. Lett., **65**(26), pp. 3410–3412.
[25] Ginder, J. M., Elie, L. D., and Davis, L. C., 1996, "Magnetic Fluid-Based Magnetorheological Fluids," Ford Motor Company, Dearborn, MI, U.S. Patent No. 5,549,837.
[26] Kittipoomwong, D., Klingenberg, D. J., and Ulicny, J. C., 2005, "Dynamic Yield Stress Enhancement in Bidisperse Magnetorheological Fluids," J. Rheol., **49**(6), pp. 1521–1538.